Steel and Composite Structures, *Vol. 56, No. 5 (2025) 383-391*
https://doi.org/10.12989/scs.2025.56.5.383

Monitoring of ground settlement around air vent of subway tunnel in metropolitan city using SBAS-InSAR and wavelet transform

Lang Fu[1a], Taeyong Park[2b], Tae Sup Yun[3c] and Hyungjoon Seo[*2]

[1]*Department of Civil Engineering and Industrial Design, University of Liverpool, Liverpool, L69 3GB, UK*
[2]*Department of Civil Engineering, Seoul National University of Science and Technology, Seoul 232, Korea*
[3]*School of Civil and Environmental Engineering, Yonsei University, 50, Yonsei-ro, Seoul, 03722, Republic of Korea*

(Received May 22, 2025, Revised June 9, 2025, Accepted June 26, 2025)

Abstract. There is a lack of quantitative constraints on the mechanism of groundwater fluctuations on the settlement of urban rail transit appurtenant structures. In this study, four air vents along the Bundang Line in Seoul, South Korea, were selected to analyze 168 Sentinel-1A C-band images acquired between July 2018 and January 2025. Using the SBAS-InSAR (Small Baseline Subset Interferometric Synthetic Aperture Radar) technique, a deformation time series covering the entire line was derived. Based on the SBAS-InSAR results, the maximum settlement rate of Bundang Line is -4.4 mm/year, and the maximum cumulative settlement is about 20 mm. Subsequently, the results of 3 wavelet transform tools to quantify the seasonal deformation of Air Vent and the underground water level show that the change of the underground water level is the primary external driver of the seasonal deformation of Air Vents, and part of the air vent deformation lags the underground water level by about 20 days. In this study, underground water level fluctuation is identified as the main driver of settlement in the Air Vent of Bundang Line, and response lags of 20-45 d are given for each section. The combination of SBAS-InSAR time series based on Sentinel-1A imagery and wavelet analysis can capture this hydrologic-deformation linkage in time with millimeter-level accuracy and monthly time delay, providing reliable data support for early warning of ground settlement along the subway tunnel and decision making for disaster mitigation.

Keywords: ground settlement; infrastructure monitoring; SBAS-InSAR; subway tunnel; wavelet transform

1. Introduction

Reasonable development and utilization of urban underground space is a key measure to alleviate the carrying pressure of rail transportation and ensure the safety of metro construction and operation. However, ground settlement, as a kind of slow-onset and cumulative geological disaster, has occurred in many cities and regions around the world, posing a serious threat to the long-term stability of underground infrastructure (Nicholls *et al*. 2021, Ye *et al*. 2016). In recent decades, along with the rapid advancement of urbanization, human activities such as over-exploitation of underground water and construction of surface and underground projects have significantly accelerated the evolution of ground settlement, which has evolved from a natural geologic process to a prominent engineering geohazard (Ding *et al*. 2021, Gezgin 2022). Especially in highly populated metropolises such as Mexico City, Shanghai and Bangkok, environmental and economic losses caused by ground settlement have been reported, posing a serious challenge to the long-term safety and sustainability of urban infrastructure (Bremard 2022, Li *et al*. 2021, Zapata-Norberto *et al*. 2025). In the process of construction and operation of urban rail transit lines, with the decline of the local underground water level and stratum disturbance, resulting in different degrees of ground settlement, which not only threatens the line structure and traffic safety, but also restricts the economic and social development of the areas along the line. The Bundang Line in Seoul, Korea, officially opened for operation on October 6, 2012, with a total length of 16 km, starting from Suseo station and ending at Cheongnyangni station. Thus, monitoring ground settlement along Bundang is of great engineering and social significance to ensure the safe and smooth operation of the metro system and the sustainable utilization of underground space.

LiDAR (Light Detection and Ranging) technology, such as laser scanning, has been applied to detect the deformation of tunnel (Becker *et al*. 2024, Alseid *et al*. 2024, Zhao *et al*. 2022, Seo *et al*. 2022). In recent years, the rapid development of InSAR technology, by virtue of its advantages of all-day, all-weather and millimeter-level accuracy, has been widely used in the field of surface deformation monitoring and disaster early warning, which provides a reliable means of fine monitoring of ground settlement along the urban rail transit lines (Chaussard *et al*. 2013, Du *et al*. 2021, Yastika *et al*. 2019). Further, with the increasing maturity of time-series InSAR technology represented by PS-InSAR (Persistent Scatterer Interferometric Synthetic Aperture Radar) and SBAS-

*Corresponding author, Ph.D. Associate Professor
E-mail: hjseo@seoultech.ac.kr
[a]Ph.D. Student
[b]Undergraduate Student
[c]Professor

ISSN: 1229-9367 (Print), 1598-6233 (Online)

Fig. 1 Bundang line and air vents

InSAR, there have been many applications of radar interferometry for millimeter-scale precision deformation monitoring of urban infrastructures such as subways (Yahui *et al*. 2020, Yang *et al*. 2022, Nur *et al*. 2024). For example, Zhang *et al*. used SBAS-InSAR and PS-InSAR based on Sentinel-1A C-band data to finely map surface deformation in Tianjin, China, and predicted the ground settlement trend with the help of a machine learning model (Zhang *et al*. 2024, Abbasi *et al*. 2024). However, the study did not delve into the mechanism of groundwater changes on urban ground settlement.

The environmental and economic damage caused by land settlement is becoming increasingly severe and poses a direct threat to the safety of urban infrastructure (Lyu *et al*. 2020). Therefore, timely prediction and assessment of ground settlement-induced damage is a key component in mitigating the impact of such geohazards. Due to the complex interactions between ground settlement processes and damage to facilities, the associated risk assessment still faces a high degree of uncertainty. Numerous studies have pointed to decreasing underground water level as one of the main factors driving urban settlement (Ahmad *et al*. 2019, Xu *et al*. 2016). Galloway and Sneed's statistics show that more than 80% of settlement events in the U.S. are closely related to underground water over-exploitation (Galloway and Sneed 2013). It is worth noting that surface ground settlement usually has a lagged response to groundwater changes, and this time-lag effect further increases the complexity of risk prediction. At present, studies coupling the spatial and temporal evolution characteristics of surface ground settlement with underground water dynamic processes are still rare.

In this study, the Bundang Line in Seoul, Korea, is used as the research object, and the SBAS-InSAR time series technique is applied to invert the surface deformation along the line, and the deformation field with high coverage and millimeter-level accuracy is obtained. On this basis, the time series deformation sequence is coupled with multi-point underground water level observation data, and the wavelet transform method is used to quantitatively reveal the period of the underground water level fluctuation on the settlement evolution and its time lag relationship, to systematically elucidate the mechanism of the settlement driven by the underground water environment (Chen *et al*. 2021, Fu *et al* 2025). This study deepens the understanding of the coupling relationship between settlement and underground water along the subway tunnel and provides a generalizable technical path and scientific basis for geohazard monitoring and risk control of similar lines.

2. Study area and data

2.1 Study area

Seoul is in the northwestern part of Korea, with an area of about 605.25 square kilometers, at 37°33′36″N, 126°59′24″E. Seoul is situated in the alluvial basin of the Han River, surrounded by mountains. The overall topography of the city is characterized by the rise of mountains in the east, north and south, and the relatively low level of the west side and the valley of the Han River. Seoul has a well-developed urban railroad network consisting of 21 rapid transit, light rail and commuter lines, one of the busiest subway systems in the world, and the largest subway system in the world, with a total track length of 940 kilometers.

The study area of this research is Bundang Line, which was officially opened for operation in October 6, 2012 from Suseo station to Cheongnyangni station, and the total length of the route is about 16 km. The details are shown in Figure 1.

Due to the recent development of numerous underground spaces and subway tunnel construction in downtown Seoul, large-scale settlement such as subway tunnel upper settlement and sinkholes has occurred frequently in the city center. Since ground settlement often occurred in the Suwon area during the Bundang Line. So ground settlement in downtown Seoul can also occur, so continuous monitoring is necessary

The 4 Air Vents selected in this study are in different landforms and land units, such as river valley, commercial area and residential area, which can provide comparative samples under multiple environmental conditions in the same Sentinel-1A field of view and help to evaluate the spatial differences in settlement distribution. In addition, the inspection records of the operator show that there are slight signs of cracking and uneven settlement near these points, which can provide comparable field information for the InSAR inversion results and lay a foundation for exploring the mechanism of underground water changes on the local deformation.

2.2 Data

In this study, the C-band VV polarized images of the Sentinel-1A satellite launched by the ESA (European Space Agency) in 2014 were selected, with the imaging mode of IW (Interferometric Wide), and the distance and azimuthal

Table 1 Satellite data parameters

Satellite	Sentinel1-A
Acquisition Mode	IW (Interferometric Wide swath)
Date Level	SLC (Single Look Complex)
Polarization Mode	VV
Orbital Direction	Descent
Angle of Incidence	34.2201
Imaging Time	Jul. 13,2018 To Jau.1,2025
Reference DEM	SRTM 30 m

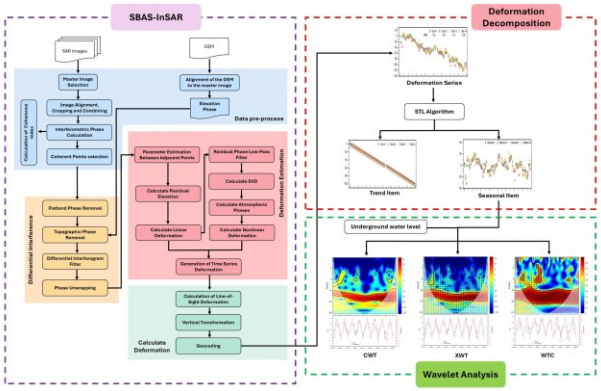

Fig. 2 Data processing workflow

resolutions of 5 m and 20 m, respectively. For the 168 images acquired between July 13, 2018, and January 1, 2025, POD (Precise Orbit Determination) data provided by the ESA was first downloaded and applied to improve the baseline estimation accuracy; The SBAS-InSAR process was then used to invert the temporal deformation of the study area. The terrain phase calculation and terrain correction are quoted from the 30 m resolution digital elevation model of NASA's SRTM (Shuttle Radar Topography Mapping) mission to ensure spatial consistency and accuracy of the interpretation results. The details are shown in Table 1.

3. Method

The aim of this study is to apply the SBAS-InSAR technique to extract the time-series deformation field along the Bundang Line in Seoul and to quantitatively assess the multiscale response of this deformation sequence to the underground water fluctuation with the help of wavelet analysis, and the overall workflow is shown in Fig. 2.

3.1 SBAS-InSAR

Berardino *et al*. proposed the SBAS-InSAR technique in 2002 (Berardino *et al*. 2002). The core idea is to select small baseline interferometric combinations in the time series to increase the number of interferometric streak maps, thus suppressing the effects of spatial de-correlation and atmospheric delay on the phase. Subsequently, the differential phases of the selected interferometric pairs are solved by the least squares method and reconstructed by integration via SVD (Singular Value Decomposition) to obtain a continuous surface deformation sequence.

In this study, S multi-temporal SAR images acquired by Sentinel-1A in the Bundang Line area of Seoul are selected and N small-baseline interferograms are generated by constraining the temporal and spatial baselines. For any interferogram ifg in the interferogram stack, the observed phase of pixel (x, y) in the radar coordinate system can be decomposed into deformation term, residual topography term, atmospheric delay term, orbit error term, and random noise term, whose specific mathematical expressions are shown in Eq. (1).

$$\begin{aligned}\phi_{obs,f}(x,y) &= \phi_{disp,f}(x,y) + \phi_{topo,f}(x,y) \\ &+\phi_{atmo,f}(x,y)+\phi_{orb,f}(x,y) + \phi_{noise,f}(x,y)\end{aligned} \tag{1}$$

where f denotes the f[th] interferogram in the stack of differential interferograms ($f \in [1,S]$) ; $\phi_{disp,f}(x,y)$ represents the phase due to pixel displacement in the LOS (Line-Of-Sight) direction of the satellite; $\phi_{topo,f}$ is a residual topographic phase error due to reference DEM inaccuracies, $\phi_{atmo,f}$ means the phase delay caused by the spatial and temporal variation of the atmospheric refractive index between two radar acquisition, and $\phi_{noise,f}$ covers then phase perturbations caused by random factors such as thermal noise and image co-alignment errors.

Using the SBAS-InSAR method, the surface deformation time series can be expressed as:

$$\begin{aligned}MV_{LOS} &= V_{LOS}\phi_{obs} = \\ M^{+}\phi_{obs}d_{LOS}^{f} &= d_{LOS}^{f} + V_{LOS}^{f+1}\Delta T^{f+1}\end{aligned} \tag{2}$$

where M is the time gap of N$(S-1)$; V_{LOS} is the line-of-sight velocity vector; d_{LOS}^{f} means the line-of-sight deformation at time T^{f}. The least-vanilla least-squares solution of Eq. (2) is obtained by solving the pseudo-inverse $M^{+}$of the matrix M by the SVD method. Finally, using the first image as the reference moment, the line-of-sight velocity vector V_{LOS} is integrated by segments, and the line-of-sight deformation sequence of each pixel during the whole observation period is accumulated step by step.

Interferogram pairs were selected using a maximum temporal baseline of 180 days and a vertical spatial baseline threshold of 150 m to ensure sufficient network redundancy while minimizing decorrelation effects. An average coherence threshold of 0.3 was used to exclude interferograms with poor phase stability. All interferograms were additionally checked manually and those affected by phase disentanglement errors or severe noise were excluded to improve the reliability of the deformation estimates. To mitigate tropospheric transport delays, atmospheric corrections were performed in this study using the InSAR GACOS (Generic Atmospheric Correction Online Service), which integrates meteorological fields from the ERA (ECMWF Re-Analysis)-Interim reanalysis and applies the terative tropospheric decomposition (ITD) model, which separates zenithal total delays into stratification components and turbulence components (Yu *et al*. 2018, Yu *et al*. 2017). The output is a set of high-resolution zenith total

tropospheric delay (ZTD) results that are interpolated to each acquisition time and used to correct the interferograms prior to time series inversion.

3.2 Wavelet analysis

Wavelet analysis is a time-frequency analysis method developed on the basis of the localization idea of the short-time Fourier transform. Different from the short-time Fourier transform with fixed window length, the time-frequency window of wavelet analysis changes adaptively with frequency, thus obtaining higher time resolution in the high-frequency band and higher frequency resolution in the low-frequency band, which is an ideal tool for dealing with non-smooth signals. In this paper, the continuous CWT (wavelet transform) is used to extract the multi-scale time-frequency features of individual signals, and the resonance intervals and phase relationships between the underground water level sequence and the air vent deformation sequence on different time scales are compared by the XWT (Cross Wavelet Transform) and WTC (Wavelet Coherence) to reveal the time-varying characteristics of the fluctuating underground water-driven deformation.

In CWT, a single time series is projected onto a two-dimensional domain constituted by the observation time and the oscillation period, and the resulting power spectrum assigns an energy intensity to each combination of time periods. The high power region corresponds to a significant periodic component within the sequence, and thus CWT is an effective tool for identifying multi-scale oscillations of a single signal (Tomás *et al*. 2020). However, CWT only reveals the periodicity of a single sequence and cannot directly assess the coupling between two sequences. To quantify the correlation and phase synchronization between underground water level fluctuation and Air Vent deformation at different scales, this study further employs WTC and XWT based on CWT analysis.

XWT is used to show the consistency and correlation of the frequency periods of two time series on different time scales by calculating the covariance distribution of the two time series in the time-frequency domain (Rateb and Kuo 2019). However, the XWT magnitude is strongly influenced by the power of each sequence itself. If one of the sequences is too powerful on a certain scale, even if the correlation between the two sequences is limited, it may produce high magnitude results and lead to misclassification. To weaken this power dominance effect, Grinsted *et al*. proposed a wavelet coherence metric to normalize the XWT results so that the coherence is limited to the 0-1 region, thus more accurately assessing the correlation strength and phase synchronization of the two sequences on all time scales (Grinsted *et al*. 2004, Abdi 2024).

4. Results

In this study, a linear buffer zone is established with a radius of 75 m centered on the Bundang Line, and the cumulative ground settlement and the average annual rate

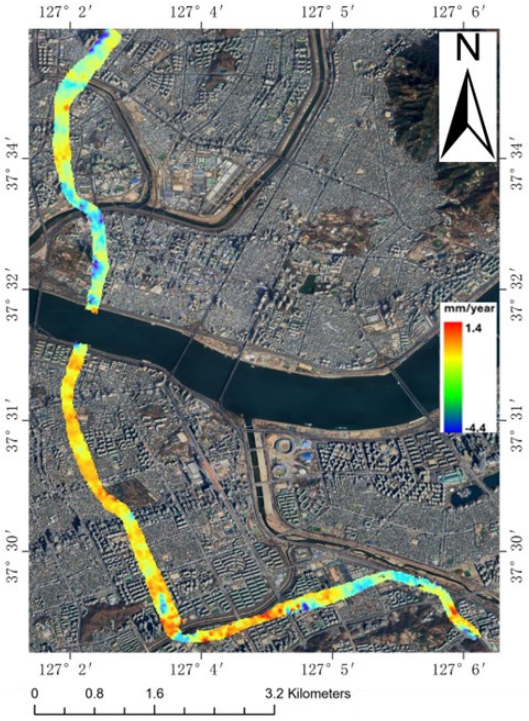

Fig. 3 Map of the average annual deformation rate of the Bundang Line

along the line are obtained during the study term. The ground deformation along the Bundang Line from 2018 to 2025 is shown in Fig. 3. Both uplifted and settled areas are observed along the segment from station Suseo to station Cheongnyangni; however, the uplift and settlement occur in different localized sections within this range. The maximum LOS settlement rate is -4.4 mm/yr, the maximum uplift rate is 1.4 mm/yr, the average value is -1.5 mm/yr, and the settlement shows a specific spatial aggregation distribution.

To quantitatively analyze the deformation patterns of the 4 selected Air Vents, a buffer zone with a radius of 15 m was constructed with the coordinates of the Air Vents as the center, and the time-series deformation recordings of all valid image elements within the buffer zone were extracted and averaged to obtain a representative deformation sequence for each Air Vent. The deformation data of the 4 air vents are shown on Fig. 4:

From Fig. 4, we can find that the maximum settlements of Air Vent 1, Air Vent 3, and Air Vent 4 all occur in July and August 2021, while the peak of Vent 8 is delayed until the end of 2024, and the peak settlements of Air Vent 3 and Air Vent 4 reach -18 mm and -20.8 mm, respectively. 20.8 mm, significantly higher than Air Vent 1 and Air Vent 8. Air Vent 1 settlement reached -14.3 mm on August 26, 2021, followed by a seasonal rebound of 6-8 mm, indicating predominantly elastic settlement. Air Vent 3 and Air Vent 4 may be more significantly affected by underground water pumping or soft soil compression.

The 4 air vent deformation series exhibit non-uniform linear characteristics throughout the observation period and can be approximately decomposed into an additive combination of the long-term trend term and the periodic

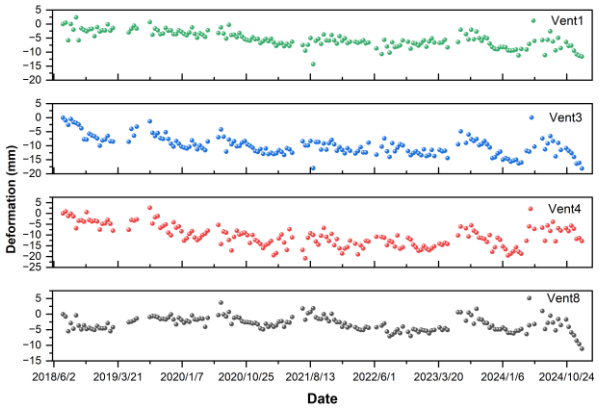

Fig. 4 Air vent time series

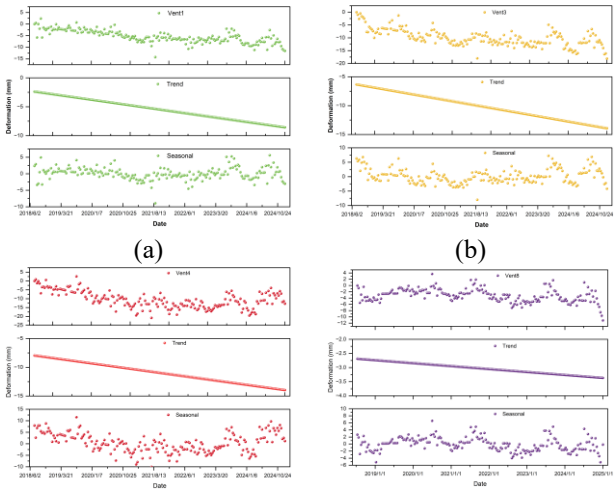

Fig. 5 STL Results

seasonal term. The long-term trend mainly reflects the irreversible deformation caused by structural self-weight and foundation consolidation, while the seasonal term corresponds to the reversible displacement caused by external hydrological loads such as precipitation recharge and underground water fluctuation.

In order to quantitatively distinguish these two types of effects, this study applies the STL (Seasonal-Trend Decomposition using Loess) method to separate each morphology series into trend and seasonal items (Cleveland *et al*. 1990). The extracted seasonal components were then analyzed in comparison with the precipitation and underground water level data of the same period, respectively, in order to assess the degree of influence of hydrological factors on air vent deformation. Wavelet analysis requires the input series to be sampled at fixed time intervals. Although Sentinel-1A has a nominal revisit period of 12 d, some of the images were missing or rejected in the SBAS-InSAR process, resulting in irregularities in the time axis of the resulting LOS deformation series. In order to restore a uniform 12-d sampling and to align with the dates of underground water level observations, polynomial interpolation of the morphology sequence is used in this paper.

This interpolation adds only constant or DC (Direct Current) components in the frequency domain and does not introduce pseudo-cycles, so it does not interfere with subsequent wavelet analysis results (Tomás *et al*. 2016). After completing the interpolation resampling, the STL decomposition is applied to the deformation sequence, and its trend item deformation and seasonal item deformation are shown in Fig. 5.

From Fig. 5, it can be found that the seasonal deformation exhibits annual cycle oscillations in all four time series, with peaks usually occurring in August-October and troughs concentrating in January-March; among them, the amplitude of Air Vent 4 is the largest, followed by Air Vent 3, and the amplitudes of Air Vent 1 and Air Vent 8 are relatively small. The STL method effectively distinguishes irreversible settlement from seasonal deformation, and Air Vent 3 and Air Vent 4 not only have higher long-term ground settlement rates but also may be more sensitive to seasonal groundwater fluctuations.

To maintain consistency with the 12-d sampling rhythm of the SBAS-InSAR deformation sequence, daily-scale records of underground water levels were first resampled, and when down sampling the water level data, the average of the previous 12 days was used as the water level data for each point. The location of the underground water measurements used was at 37°31'1.91" N, 127° 2'43.18" E. Seasonal deformation of the 4 air vents plotted against the underground water level data is shown in Figure 6.

It can be noticed from Fig. 6. From 2018 to 2025 the seasonal deformation of both underground water level and Air Vent is dominated by the annual cycle. The underground water level generally rises with abundant water recharge from July to October and decreases with evapotranspiration from January to March of the following year. The deformation curves show an inverse response, with ground settlement slowing down significantly or rebounding slightly when the water table rises and accelerating when the water table falls. There is a certain periodicity and correlation between the seasonal deformation of the Air Vent and the underground water level data. To further discover the correlation between them, wavelet analysis is used to analyze their correlation and hysteresis in the time-frequency domain.

Continuous wavelet transformations were performed on the seasonal deformation and underground water levels of the 4 Air Vents to show their time-frequency characteristics. The continuous wavelet transformation is represented as a two-dimensional graph, i.e., continuous wavelet power spectrum, whose two axes represent the time moments and periods (or frequencies) of specific modes, as shown in Fig. 7. Thus, locations with higher mode values in the continuous wavelet transform usually indicate localized signals with significant similarity to wavelets of specific frequencies.

In the wavelet power spectrum of Fig. 7, the horizontal axis is the date of observation, the vertical axis is the frequency, and the color mapping indicates the energy intensity, with red corresponding to the power peaks and blue to the power valleys. The thick black solid line circles the 5 % significance boundary with respect to the red noise

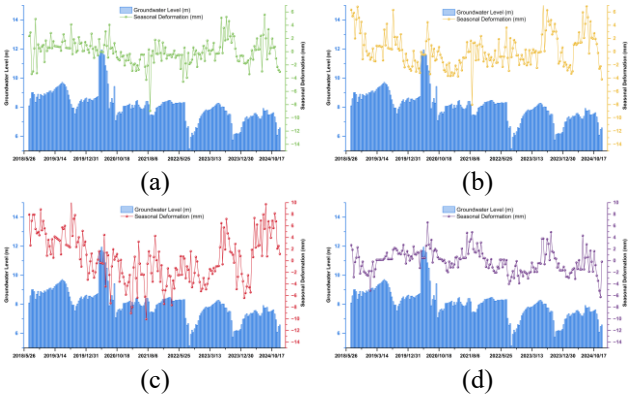

Fig. 6 Seasonal deformation of underground water levels

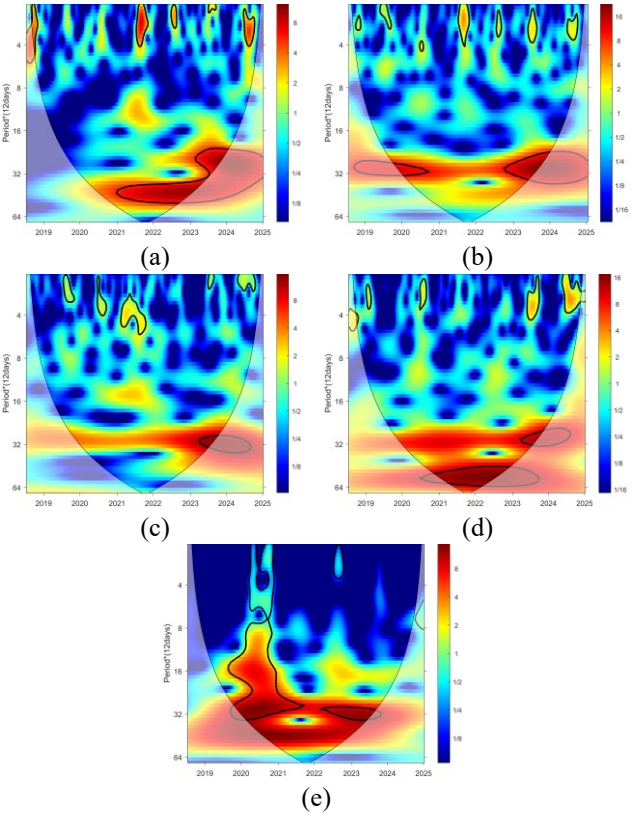

Fig. 7 CWT results for different time series data. (a) Seasonal deformation of Air Vent 1, (b) Seasonal deformation of Air Vent 3, (c) Seasonal deformation of Air Vent 4, (d) Seasonal deformation of Air Vent 8, (e) Underground water level

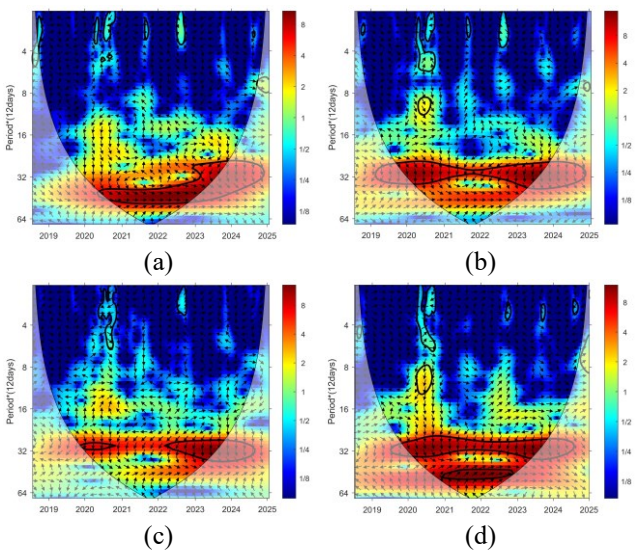

Fig. 8 XWT results for different time series data; (a) (b) (c) (d) denote the cross-wavelet power spectra of seasonal deformation and underground water level for Air Vent1, Air Vent3, Air Vent4, and Air Vent8, respectively

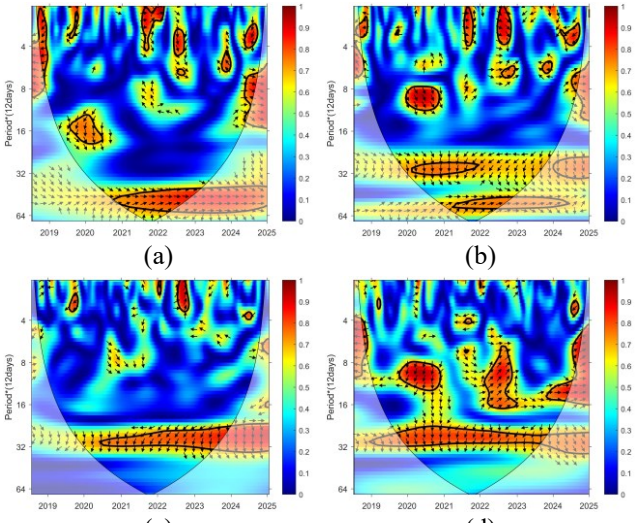

Fig. 9 WTC results for different time series data; (a) (b) (c) (d) Crossed wavelet energy spectra of seasonal deformation and underground water level for Air Vent1, Air Vent3, Air Vent4, and Air Vent8, respectively

background, and only the power peaks within this contour are statistically plausible. The area with the translucent mask in the figure is the COI (Cone of Influence), and the power spectrum outside the COI is not included in the discussion of the results due to edge effects.

To further evaluate the driving effect of underground water fluctuation on deformation and its hysteresis characteristics, XWT and WTC will be used next. XWT can extract the common power structure of the two sequences in the time-frequency domain, whereas WTC, by normalizing the results of XWT, can give the coherence in the 0-1 region, and then determine the correlation strength and phase difference between the two in each period band. The results are shown in Figs. 8 and 9.

In the XWT and WTC results, arrows pointing to the right indicate a positive correlation between Air Vent seasonal deformation and underground water level, and arrows pointing to the left indicate a negative correlation. Arrows pointing diagonally at 45° indicate that Air Vent seasonal deformation or changes in underground water level are about a quarter of a cycle ahead of each other.

5. Discussions

Continuous wavelet power spectra shown in Fig. 7 reveals the main oscillatory scales and time-varying characteristics of the seasonal deformations of the underground water level and Air Vents. The annual cycle energy of the underground water level is most concentrated in 2019-2021, and then gradually decreases; the annual cycle power of the Air Vents deformation increases significantly from 2022 onwards, especially in Vent 1 and Vent 8, which show continuous high-energy region, while Vent 3 and Vent 4 show two discrete peaks in 2019-2020 and 2023-2024, and the annual cycle power of the Air Vents deformation increases significantly in 2020 and 2023-2024. 2020 and 2023-2024 with two discrete peaks. This temporal mismatch implies that there is a seasonal-to-annual scale lag in the transmission of underground water oscillations to foundation deformation and may be influenced by zonal geologic conditions or pumping intensity. In addition to the annual scale, the underground water level also shows intermittent semiannual energy peaks in the 12~20 × 12 d (0.4~0.7 year) band.

From the XWT results, it can be found that the underground water level and the four Air Vents deformation sequences show continuous and concentrated resonance energies in the annual cycle band of 30 to 35 × 12 d (about 0.9-1.1 yr), and the corresponding phase arrows are generally pointing to the left and slightly deflected downward, which suggests that the deformation and the underground water level are in a stable inverse-phase relationship with a lag of 15 to 40 d between the deformation and the water level. to about 40 d. From 2019 to 2021, this power is brightest across all Air Vents, indicating that underground water oscillations drive Air Vents deformation the most in that year. From 2022 onwards, the power of Air Vent 1 and Air Vent 8 is enhanced, while the energy of Air Vent 3 and Air Vent 4 is slightly split. In the higher-frequency 12 to 20 × 12 d interval, significant resonance occurs only in Vent 3 (2020) and Vent 8 (2020-2021) and is of shorter duration, suggesting that this higher-frequency signal is effectively captured only in regions with better infiltration conditions, and may be related to localized underground water pumping rhythms or short-term water-level fluctuations transmitted directly to the foundation.

The WTCs in Fig. 9 were normalized and the annual-scale coefficients were above 0.7 in all four Air Vents and passed the 5 % red noise significance test, which confirms that the annual oscillation of the underground water is the primary external driver of the seasonal deformation of the Air Vents. The phase angles further quantify the lag lengths: Air Vent 4 has the smallest arrow declination of about -0.20 π radians, which corresponds to a lag of about 20 days; Air Vent 3 has an arrow declination of about -0.27 π radians, which corresponds to a lag of about 30 days; and Air Vent 1 and Air Vent 8 have declinations of nearly Air Vent 1 and Air Vent 8 have deflections close to -π/6 radians, indicates that changes in the underground water level lead the deformation response by about 40 to 45 days. At the semiannual scale, only the localized energy zones of Air Vent 3 and Air Vent 8 pass the significance test with a lag of less than 10 days, suggesting that the triggering of Air Vents settlement by changes in the underground water table due to short-term heavy rainfall needs to satisfy certain infiltration conditions rather than being widespread along the line.

In addition to the above findings, it is important to recognize the limitations of the methodology employed. In dense urban environments, the SBAS-InSAR technique may suffer from temporal de-correlation, especially in areas of non-persistent scatterers or during prolonged monitoring. The presence of mixed pixels may also introduce uncertainty in the phase signal due to the presence of complex surface types (roofs, roads, and vegetation) within the same resolution cell. In addition, the wavelet-based analysis rests on the assumption of a uniformly sampled time series. Although interpolation is used to achieve regular sampling intervals, this step may suppress short-term variations. Edge effects inherent in the wavelet transform, especially outside the cone of influence, can also affect the reliability of frequency localization features.

6. Conclusions

SBAS-InSAR was used to monitor the Bundang Line and obtain the LOS deformation time series of 4 air vents along the Bundang Line from 2018 to 2025.The SBAS-InSAR monitoring results show that the settlement is mainly concentrated in the northern area, and most of the southern area is uplifted. Combining the air vent seasonal deformation sequences obtained by SBAS-InSAR and STL methods with the underground water level monitoring records, this study quantitatively reveals the characteristics of the response of the Bundang Line air vent settlement to the underground water cycle fluctuations by using the CWT, XWT, and WTC methods. The analysis results show that the amplitude of underground water level is the largest from 2019 to 2021, and the annual scale coupling is the most significant in Air Vent. From 2022 onwards, the energy of the annual region of Air Vent 1 and Air Vent 8 falling in the interval of 1-year cycle is significantly enhanced, while Air Vent 3 and Air Vent 4 are slightly split, which reflects the influence of underground water fluctuation on the deformation of different zones. The phase angle of the annual cycle shows that Air Vent 4 has the fastest response to the water level change with a lag of about 20 d, Air Vent 3 with a lag of about 30 d, and Air Vent 1 and Air Vent 8 with a lag of about 40 to 45 d, which suggests that the water-soil transfer path is longer in the softer sections at both ends. The wavelet analysis quantitatively portrays the time lag and spatial difference of the structural settlement caused by the change of underground water level, which provides a basis for the monitoring and early warning of the settlement of the Bundang Line Air Vent and provides a usable methodological framework for the future study of the groundwater-settlement coupling of urban rail transit lines.

Acknowledgements

This work was supported by the National Research Foundation of Korea (NRF) grant funded by the Korea government (MSIT) (No. RS-2021-NR060085).

Reference

Abbasi, M., Namadchi, A. H., Abbasi, M. and Abbasi, M. (2024), "Evaluation of machine learning algorithms in tunnel boring machine applications: A case study in Mashhad metro line 3", *Geo-Eng*., **15**(1), 28, https://doi.org/10.1186/s40703-024-00228-y.

Abdi, Y. (2024), "Investigation of the strength behavior and failure modes of layered sedimentary rocks under Brazilian test conditions", *Geo-Eng*., **15**(1) 6, https://doi.org/10.1186/s40703-024-00208-2.

Ahmad, W., Choi, M., Kim, S. and Kim, D. (2019), "Detection of land subsidence and its relationship with land cover types using ESA Sentinel satellite data: a case study of Quetta Valley, Pakistan", *Int. J. Remote Sensing*, **40**(24), 9572-9603.

Alseid, B., Chen, J., Huang, H. and Seo, H. "R-C-D-F machine learning method to measure for geological structures in 3D point cloud of rock tunnel face", *Tunnell. Underg. Space Technol*., **154**, 106071.

Becker, D., Raddatz, L., Roussel, C. and Klonowski, J. (2024), "Analysis methods for deformation detection using TLS and UAS data on the example of a landslide simulation", *Geo-Eng*., **15**(1), 9, https://doi.org/10.1186/s40703-023-00203-z.

Berardino, P., Fornaro, G., Lanari, R. and Sansosti, E. (2002), "A new algorithm for surface deformation monitoring based on small baseline differential SAR interferograms", *IEEE Transact. Geosci. Remote Sensing*, **40**(11), 2375-2383.

Bremard, T. (2022), "Monitoring land subsidence: The challenges of producing knowledge and groundwater management indicators in the Bangkok metropolitan region, Thailand", *Sustainability*, **14**(17), 10593.

Chaussard, E., Amelung, F., Abidin, H. and Hong, S.-H. (2013), "Sinking cities in Indonesia: ALOS PALSAR detects rapid subsidence due to groundwater and gas extraction", *Remote Sensing Environ.*, **128**, 150-161.

Chen, C., Seo, H. and Zhao, Y. (2021), "A novel pavement transverse cracks detection model using WT-CNN and STFT-CNN for smartphone data analysis", *Int. J. Pave. Eng*., **23**(12), 4372-4384.

Cleveland, R.B., Cleveland, W.S., McRae, J.E. and Terpenning, I. (1990), "STL: A seasonal-trend decomposition. *J. off. Stat*, **6**(1), 3-73.

Ding, P., Jia, C., Di, S., Wu, J. and Wei, R. (2021), "Analysis and evaluation of land subsidence along linear engineering based on InSAR data", *Ksce J. Civil Eng.*, **25**(9), 3477-3491.

Du, Y., Fu, H., Liu, L., Feng, G., Peng, X. and Wen, D. (2021), "Orbit error removal in InSAR/MTInSAR with a patch-based polynomial model", *Int. J. Appl. Earth Observation Geoinform.*, **102**, 102438.

Fu, L., Ahmed, Z., Kim, D. and Seo, H. (2025), "Monitoring dynamic behavior of bridges through wavelet transform of laser doppler vibrometer signal", *J. Civil Struct. Health Monit*., 1-16. https://doi.org/10.1007/s13349-024-00901-x.

Galloway, D.L. and Sneed, M. (2013), "Analysis and simulation of regional subsidence accompanying groundwater abstraction and compaction of susceptible aquifer systems in the USA", *Boletín de la Sociedad Geológica Mexicana*, **65**(1), 123-136.

Gezgin, C. (2022), "The influence of groundwater levels on land subsidence in Karaman (Turkey) using the PS-InSAR technique", *Adv. Space Res.*, **70**(11), 3568-3581.

Grinsted, A., Moore, J.C. and Jevrejeva, S. (2004), "Application of the cross wavelet transform and wavelet coherence to geophysical time series", *Nonlinear Processes Geophys.*, **11**(5/6), 561-566.

Li, M.-G., Chen, J.-J., Xu, Y.-S., Tong, D.-G., Cao, W.-W. and Shi, Y.-J. (2021), "Effects of groundwater exploitation and recharge on land subsidence and infrastructure settlement patterns in Shanghai", *Eng. Geology*, **282**, 105995.

Lyu, H.-M., Shen, S.-L., Zhou, A. and Yang, J. (2020), "Risk assessment of mega-city infrastructures related to land subsidence using improved trapezoidal FAHP", *Sci. Total Environ.*, **717**, 135310.

Nicholls, R.J., Lincke, D., Hinkel, J., Brown, S., Vafeidis, A.T., Meyssignac, B., Hanson, S.E., Merkens, J.-L. and Fang, J. (2021), "A global analysis of subsidence, relative sea-level change and coastal flood exposure", *Nature Climate Change*, **11**(4), 338-342.

Nur, A.S., Nam, B.H., Choi, S. and Kim, Y.J. (2024), "Monitoring of ground subsidence using PS-InSAR technique in the Southeast Texas (SETX) Region", *Geo-Eng*., **15**, 13, https://doi.org/10.1186/s40703-024-00215-3.

Rateb, A. and Kuo, C.-Y. (2019), "Quantifying vertical deformation in the Tigris–Euphrates basin due to the groundwater abstraction: Insights from GRACE and Sentinel-1 satellites", *Water*, **11**(8), 1658.

Seo, H., Zhao, Y. and Chen, C. (2022), "Displacement mapping of point clouds for retaining structure considering shape of sheet pile and soil fall effects during excavation", *J. Geotech. Geoenviron. Eng*., **148**(5), 04022016

Tomás, R., Li, Z., Lopez-Sanchez, J.M., Liu, P. and Singleton, A. (2016), "Using wavelet tools to analyse seasonal variations from InSAR time-series data: A case study of the Huangtupo landslide", *Landslides*, **13**, 437-450.

Tomás, R., Pastor, J. L., Béjar-Pizarro, M., Bonì, R., Ezquerro, P., Fernández-Merodo, J.A., Guardiola-Albert, C., Herrera, G., Meisina, C. and Teatini, P. (2020), "Wavelet analysis of land subsidence time-series: Madrid Tertiary aquifer case study", *Proceedings of the International Association of Hydrological Sciences*, **382**, 353-359.

Xu, Y.-S., Shen, S.-L., Ren, D.-J. and Wu, H.-N. (2016), "Analysis of factors in land subsidence in Shanghai: A view based on a strategic environmental assessment", *Sustainability*, **8**(6), 573.

Yahui, Q., Weiping, B., Zhiyi, B., Changqing, L., Kuo, Z. and Bo, L. (2020), "Urban underground rail transit settlement and disaster monitoring based on InSAR", *Bull. Surveying Mapping*, **2**, 107.

Yang, M., Wang, R., Li, M. and Liao, M. (2022), "A PSI targets characterization approach to interpreting surface displacement signals: A case study of the Shanghai metro tunnels", *Remote Ssensing Environ.*, **280**, 113150.

Yastika, P., Shimizu, N. and Abidin, H. (2019), "Monitoring of long-term land subsidence from 2003 to 2017 in coastal area of Semarang, Indonesia by SBAS DInSAR analyses using Envisat-*ASAR, ALOS-PALSAR, and Sentinel-1A SAR data*", *Adv. Space Res.*, **63**(5), 1719-1736.

Ye, S., Xue, Y., Wu, J., Yan, X. and Yu, J. (2016), "Progression and mitigation of land subsidence in China", *Hydrogeol. J.*, **24**(3), 685.

Yu, C., Li, Z., Penna, N. T. and Crippa, P. (2018), "Generic atmospheric correction model for interferometric synthetic aperture radar observations", *J. Geophys. Res. Solid Earth*, **123**(10), 9202-9222.

Yu, C., Penna, N.T. and Li, Z. (2017), "Generation of real-time mode high-resolution water vapor fields from GPS observations", *J. Geophys. Res. Atmosp.*, **122**(3), 2008-2025.

Zapata-Norberto, B., Morales-Casique, E., Contreras-Galván, R.

and Ramos-Leal, J.A. (2025), "Land subsidence in Mexico City: New insights from field data and numerical modeling", *Groundwater Sustain. Develop.*, **29**, 101432.

Zhang, J., Kou, P., Tao, Y., Jin, Z., Huang, Y., Cui, J., Liang, W. and Liu, R. (2024), "Urban ground subsidence monitoring and prediction using time-series InSAR and machine learning approaches: a case study of Tianjin, China", *Environ. Earth Sci.*, **83**(16), 473.

Zhao, Y., Seo, H. and Chen, C. (2022), "Displacement analysis of point cloud removed ground collapse effect in SMW by CANUPO machine learning algorithm", *J. Civil Struct. Health Monit*., **12**, 447-463.